Further results on the development of a novel VTOL aircraft, the Anuloid. Part I: Aerodynamics

Marco Petrolo[*1], Erasmo Carrera[1a], Gaetano Iuso[2b], Zdeněk Pátek[3c] and Zdenek Janda[4d]

[1]*MUL² Group, Department of Mechanical and Aerospace Engineering, Politecnico di Torino, Corso Duca degli Abruzzi 24, Torino, Italy*
[2]*Department of Mechanical and Aerospace Engineering, Politecnico di Torino, Corso Duca degli Abruzzi 24, Torino, Italy*
[3]*VZLÚ Aerospace Research and Test Establishment, Prague, Czech Republic*
[4]*FESA s.r.o., Prague, Czech Republic*

Abstract. This paper presents the main outcomes of the preliminary development of the Anuloid, an innovative disk-shaped VTOL aircraft. The Anuloid has three main features: lift is provided by a ducted fan powered by a turboshaft; control capabilities and anti-torque are due to a system of fixed and movable surfaces that are placed in the circular internal duct and the bottom portion of the aircraft; the Coanda effect is exploited to enable the control capabilities of such surfaces. In this paper, results from CFD analyses and wind tunnel tests are presented. Horizontal and vertical flights were considered, including accelerated flight. Particular attention was paid to the experimental analysis of the Coanda effect via a reduced scale 3D printed model. The results suggest that the Coanda effect is continuously present at the lower surface of the Anuloid and may be exploited for the control of the aircraft. Also, very complex 3D flows may develop around the aircraft.

Keywords: VTOL; Coanda effect; CFD; wind tunnel

1. Introduction

The present paper is a companion work of Petrolo *et al*. (2014) in which the early development of a disk-shaped Vertical Take-Off and Landing (VTOL) aircraft hereinafter referred to as the Anuloid was presented. In this aircraft, the ducted airflow from a fan powered by a turboshaft contributes to the lift generation together with the Coanda effect that is also exploited for the flight control. This paper presents further developments, with particular attention paid to CFD and wind tunnel tests. Some of the most important aircraft exploiting ducted turbojet airflows and the

*Corresponding author, Assistant Professor, E-mail: marco.petrolo@polito.it
[a]Professor, E-mail: erasmo.carrera@polito.it
[b]Professor, E-mail: gaetano.iuso@polito.it
[c]Researcher, E-mail: patek@vzlu.cz
[d]Researcher, E-mail: zdenek.janda@centrum.cz

(a) 3D view   (b) Cross-sectional view

Fig. 1 Anuloid geometry

Coanda effect are briefly introduced hereinafter. More comprehensive reviews of VTOLs can be found in Petrolo *et al*. (2014), (2016).

In the Anuloid, the vertical and the horizontal thrust can be obtained by ducting the turbojet airflow. Whereas, the control of the airflow can be realized by movable vanes exploiting the so-called Coanda effect. Such effect can be described as follows: "a stream of air at high velocity will attach to a curved surface rather than follow a straight line in its original direction" (Barlow *et al*. 2009). One of the first examples of aircraft based on the lift production through a ducted airflow was the VZ-9AV "Avrocar" (1950) (Lindenbaum and Blake). The Avrocar had an annular wing obtained upon rotating an airfoil about its leading edge. Three turbojet engines were located on the leading edge and drove a central rotor whose aspired air was mixed with the exhaust gases and ducted to a peripheral annular nozzle. This ducted flow followed the nozzle geometry (by exploiting the Coanda effect) and was oriented underneath the Avrocar, thus promoting lift. Unfortunately, this aircraft suffered from the ground effect and uncontrolled pitch. The ducted airflow and Coanda effect have recently found increased application in VTOL unmanned aerial vehicles (UAV) (Crivoi *et al*. 2013).

A propeller embedded into the aircraft structure (fuselage or wing) leads to the creation of a ducted fan that enhances the generated thrust with respect to the unshrouded propellers of the same size. This improvement is provided by the reduction of the tip loss and to the optimization of the airflow velocity and pressure through an accurate duct design (Fite 2013). Moreover, the duct can host passive or active acoustic dampers for reducing the noise of the engine. Examples are the AirMule, the Centaur and the X-Hawk. The airframe of these aircraft only marginally provides aerodynamic lift; the ducted fans operate as powered lift generators for these wingless configurations. All ducted fans are driven by the same engine, which, on the one hand, reduces the propulsion system weight but, on the other hand, requires the use of power transmission mechanisms requiring adequate maintenance.

From these studies, it appears that two synergic lifting mechanisms can be activated by the Coanda effect by ducting the airflow at high velocity over a curved surface,

• The curved surface can redirect the airflow downwards, this leads to the production of vertical thrust.

• The deflected airflow can entrain surrounding air, inducing a low-pressure region above the body and thus lift.

The first way of producing lift has been demonstrated to be largely dominant over the second one. Moreover, the deflection of the downstream should permit the control of pitch, roll and yaw. It is also interesting to report research activities aimed at reducing rotor downwash on tilt rotor aircraft using the Coanda effect (Angle *et al*. 2006).

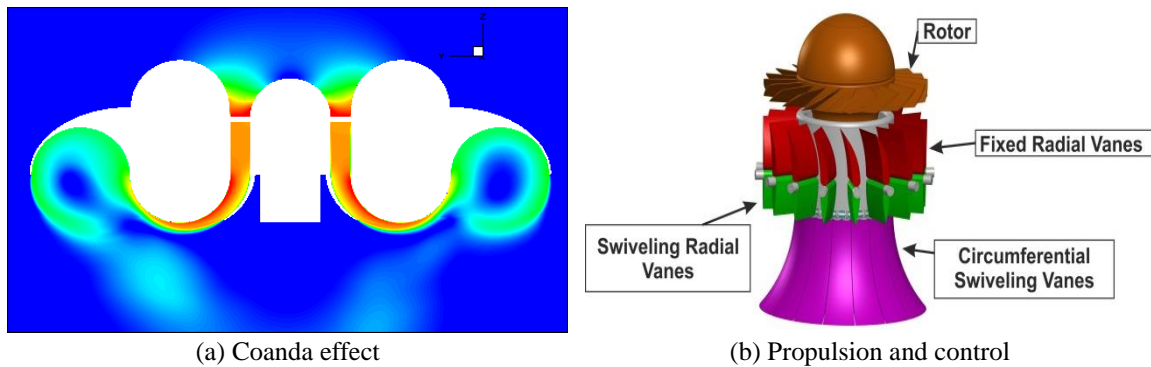This paper is organized as follows: the Anuloid is briefly described in Section 2, CFD analyses

(a) Coanda effect   (b) Propulsion and control

Fig. 2 Anuloid main characteristics

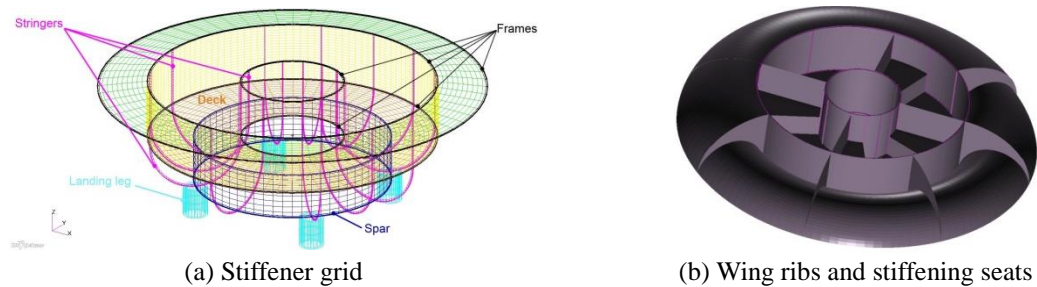(a) Stiffener grid   (b) Wing ribs and stiffening seats

Fig. 3 Anuloid main structural frame

are shown in Section 3, experimental wind tunnel results are given in Section 4, and the main conclusions are drawn in Section 5.

2. The Anuloid aircraft

The Anuloid is a disk-shaped VTOL aircraft, see Fig. 1. The outer diameter is 5 m, and the maximum take-off weight is about 1200 kg. The propulsive system is a turboshaft engine in its center that drives a ducted rotor. Only one propulsion system is implemented for lift and cruise with a more favorable payload-to-empty weight ratio. The typical Anuloid operating scenarios are emergency missions and civil transportations in urban areas. The cruise speed should fall in the 100-200 km/h range.

A robust Coanda effect is expected through the inner duct and along the bottom side of the circumferential wing. Fig. 2(a) shows a CFD analysis in which the Coanda effect is clearly visible. More details about this analysis are given in the next sections. Fig. 2(b) shows the rotor configuration and the system of fixed and movable blades that is placed in the inner vane of the aircraft. The combined exploitation of Coanda and the inner vane components are fundamental for the Anuloid. In fact,

• The flow from the rotor goes through the fixed and the swiveling radial vanes that eliminate the rotor torque and provide yaw control by controlling the swirl of the flow.

• The individual swiveling of the circumferential vanes can control the tilting of the aircraft by local variations of the resistance to the airflow.
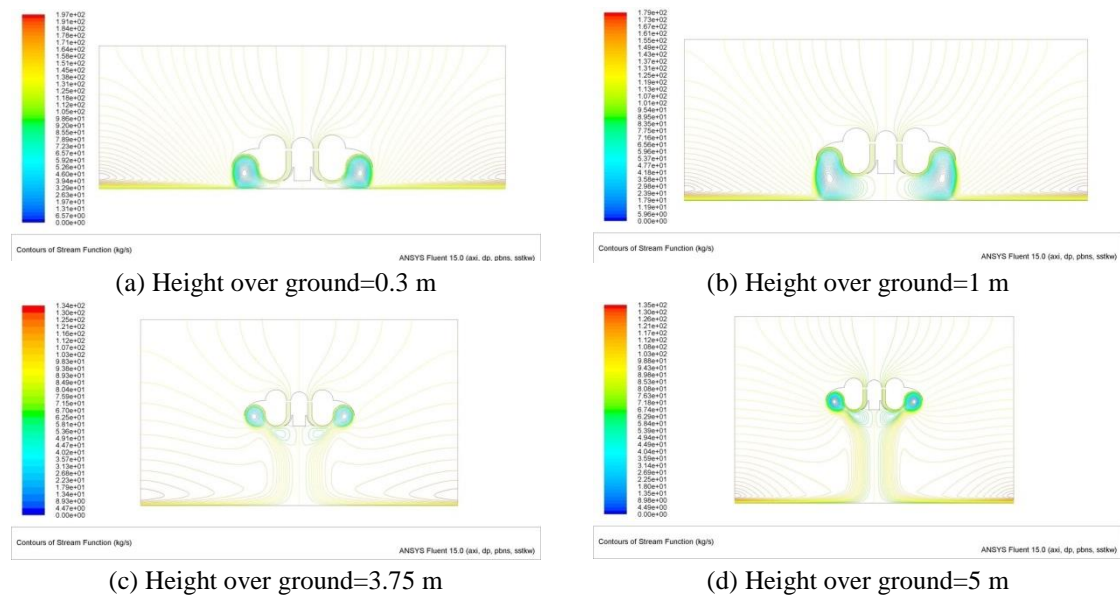
(a) Height over ground=0.3 m

(b) Height over ground=1 m

(c) Height over ground=3.75 m

(d) Height over ground=5 m

Fig. 4 Vertical flight streamlines

• The Anuloid can head in the direction of tilting. Control forces and moments for the Anuloid are obtained through the manipulation of the ducted airflow and the Coanda effect.

Furthermore, additional lift could be produced by the Coanda effect as soon as the flow remains attached to the curved bottom surface of the aircraft. However, this aircraft may be assumed as wingless since lift is essentially power generated, the circular fuselage being supposed to produce only marginal additional lift during the cruise.

The structural frame is made of fiber reinforced composites and sandwich panels. Fig. 3 shows the three main structural components, namely

• A grid of circumferential and radial stiffeners as the main structural frame.
• A set of seats with structural purposes to provide additional rigidity.
• A set of radial ribs along the circumferential wing that enhance the modal characteristics of the aircraft and avoid aeroelastic phenomena.

Preliminary structural analyses and sizing were carried out in Nastran as shown in Petrolo *et al*. (2014). Results proved that the structural and aeroelastic design of the Anuloid are not particularly critical, and weight requirements can be met.

3. CFD analysis of internal and external flows

3.1 Vertical flight

This section deals with the CFD analysis of the vertical flight to investigate the Coanda effect strength. Analyses of the power requirements for take-off and landing can be found in Petrolo *et al*. (2014). Ansys Fluent 15.0 was used. The following input data set was adopted: SST k-omega turbulence model, steady state method used, diameter of Anuloid=5.2 m, diameter of rotor=1.2 m, diameter of the central vane=0.8 m, flow through the rotor=100 m^3/s.
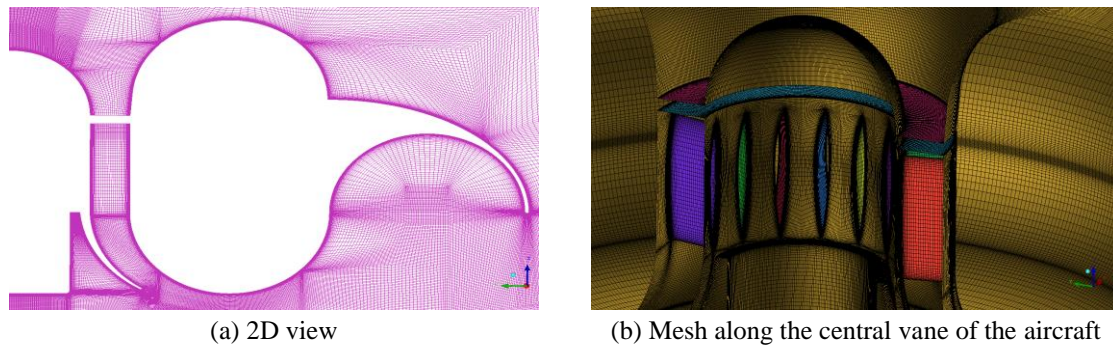
(a) 2D view

(b) Mesh along the central vane of the aircraft

Fig. 5 CFD mesh for the horizontal flight analysis

Table 1 Yaw moment and coefficient (M_N and C_N)

$\dot{m}$, kg/s	δ_B, °	M_N, Nm	C_N
80	0	-164	-0.00270
122.5	0	73	0.00120
80	10	2064	0.03390
122.5	10	4200	0.06900

Fig. 4 shows streamline distributions for different heights. From the pictures of streamlines, it is clear that the Coanda effect is very strong and generates large toroidal whirls touching the ground from basic take-off/landing position up to about 3.75 m. The shrinking of this large toroidal whirl at this height (and above) should lead to a change of the rotor lift, the fuselage (pressure) lift, the total lift, and the required power to values characteristic of hover flight in free air.

3.2 Horizontal flight

This section deals with the horizontal flight analysis of the aircraft. In (Petrolo *et al*. 2014), CFD analyses were carried out by replacing the set of individually separated control vanes with a continuous smoothly deformable collar without distinguished individual vanes. In this paper, the individual control vanes were taken into account. A half of the aircraft was modeled and located in a half-cylinder domain of radius 75 m, and height 100 m. The computational mesh had 60 million hexahedral elements. At least 35 million elements were used for the boundary layers of the Anuloid body and blades. The thickness of the first layer of elements is about 1 mm. This 1 mm thick layer was split into 33 layers. The height of the first element (on the wall) is 0.0025 mm. The height progression ratio is 1.2. Fig. 5 shows the mesh adopted. EDGE, an FOI's in-house computational fluid dynamic (CFD) program package, was used. EDGE is a finite-volume Navier-Stokes solver for unstructured meshes.

The following physical conditions were considered: angle of attack, $\alpha=0°$; velocity, 30 m/s; mass flow, 80 kg/s and 122.5 kg/s. Two blade deflection angles were considered (δ_B), 0° and 10°.

Figs. 6 and 7 show pressure and Mach distributions for two different sets of input parameters. Table 1 presents the yaw moment values and coefficients for various blade deflections and mass flows. The results suggest that:
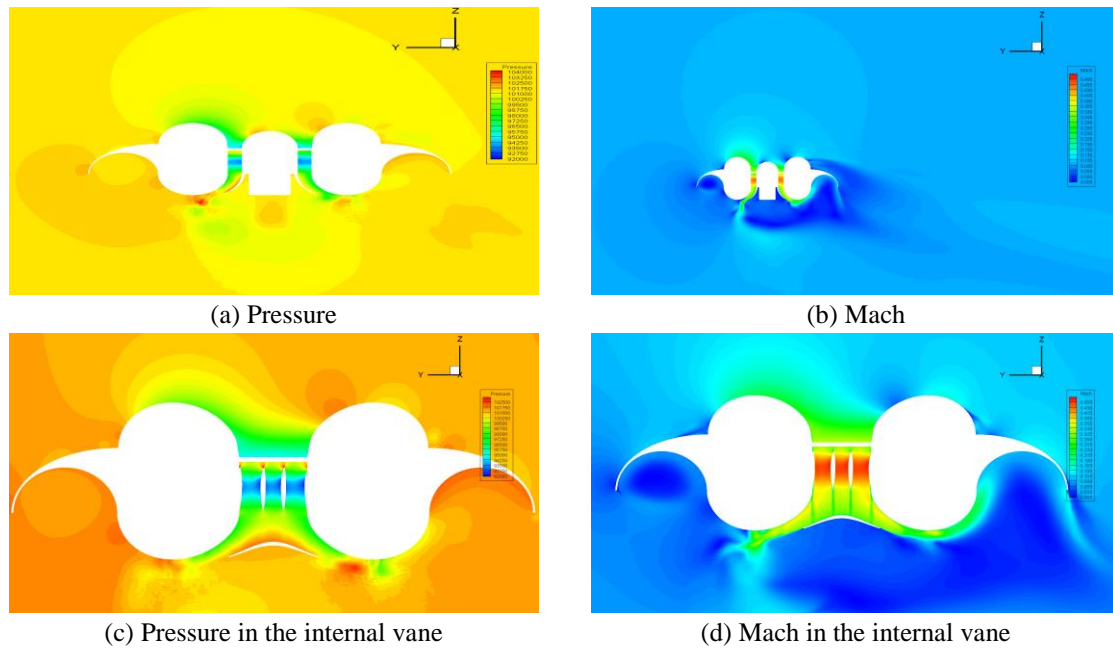
(a) Pressure

(b) Mach

(c) Pressure in the internal vane

(d) Mach in the internal vane

Fig. 6 Horizontal flight pressure and mach distributions, δ_B=0, 80 kg/s

(a) Pressure

(b) Mach

(c) Pressure in the internal vane
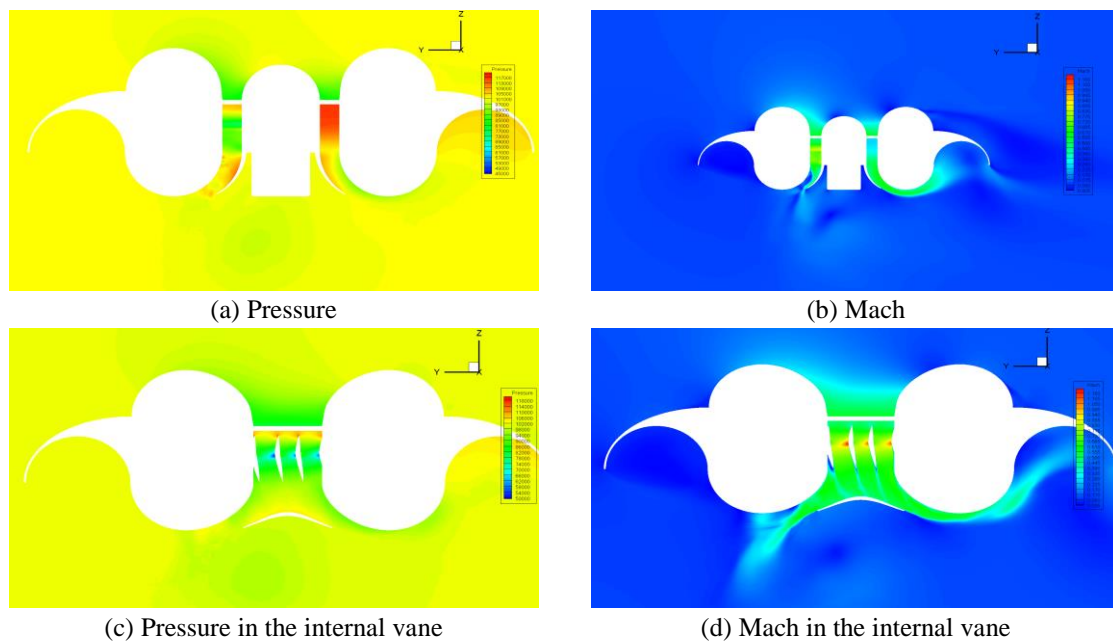

(d) Mach in the internal vane

Fig. 7 Horizontal flight pressure and mach distributions, δ_B=10, 122.5 kg/s

• There may be unstable flow regions around the Anuloid.

• The blade deflection angles and the mass flow influence the yaw moment coefficient. Higher the mass flow or the blade angle, higher the resulting yaw moment.
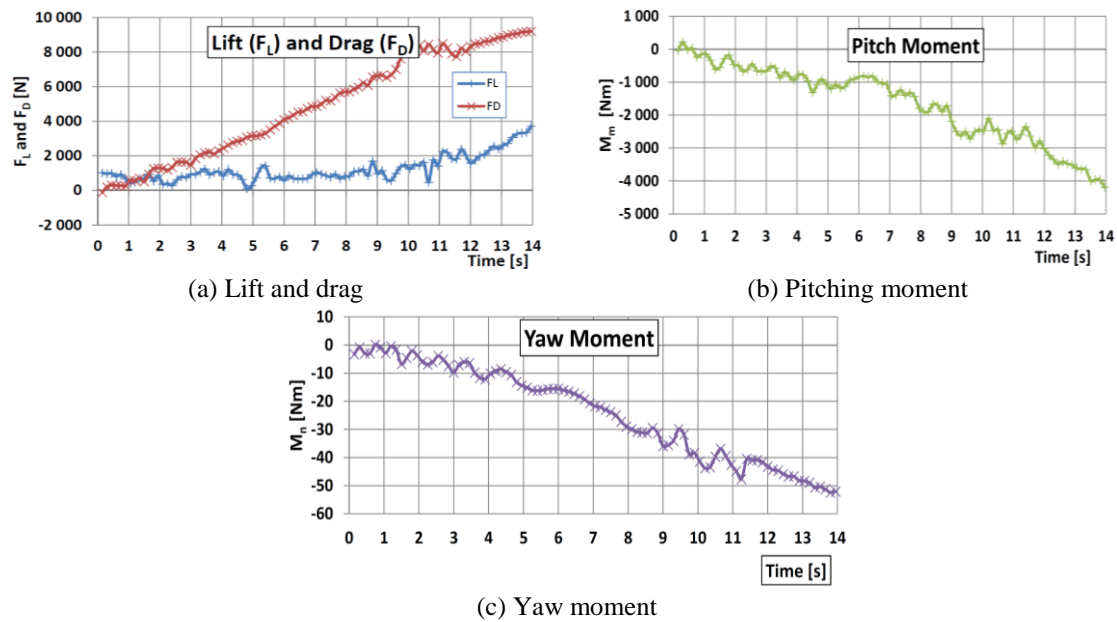
(a) Lift and drag

(b) Pitching moment

(c) Yaw moment

Fig. 8 Accelerated flight aerodynamic forces and moments, α=-10°

3.3 Accelerated horizontal flight

This section presents the results of the accelerated horizontal flight analysis that was carried out via the EDGE code. The following input parameters were used: α=-10°, mass flow=122.5 kg/s. A constant acceleration of 2 m/s^2 was considered (from 0 to 28 m/s). The computational grid shown in Fig. 5 was used. Fig. 8 shows the aerodynamic forces and moments for a nose-down configuration. The irregularities in the development of the forces and moments could be caused be certain irregularities in the flow under the bottom of the aircraft. Moreover, another source of irregularities may be due to the calculation of the resulting forces and moments that were computed by integration of the pressure.

4. Aerodynamic experimental activity

The experimental activity focused on the wind tunnel investigation of the aerodynamic characteristics of the aircraft and the analysis of the Coanda effect. The former was carried out on a 1:5 scale model, whereas the latter on a 1:22 scale model. The smaller model was 3D printed.

4.1 Aerodynamic coefficients

Forces and moments were evaluated using a six component external balance and pressure distributions using two scanivalves pressure devices. The aircraft model was tested without the fan due to several difficulties related to its mounting in the test section. Therefore, the aerodynamic characterization that follows is partial but can give fundamental, preliminary insight on the aerodynamic of the basic shape of the body.

(a) Aircraft in the test section

(b) Model equipped for the installation
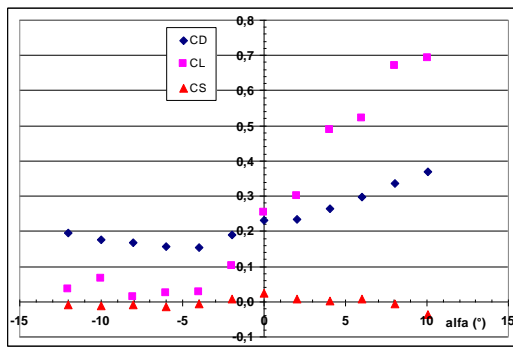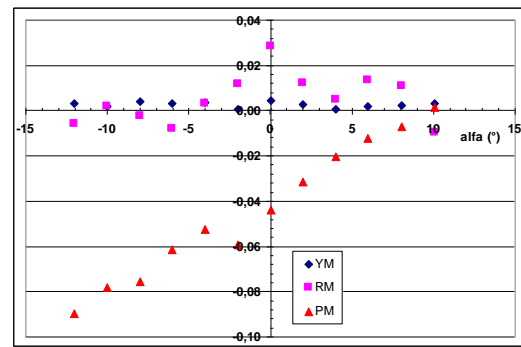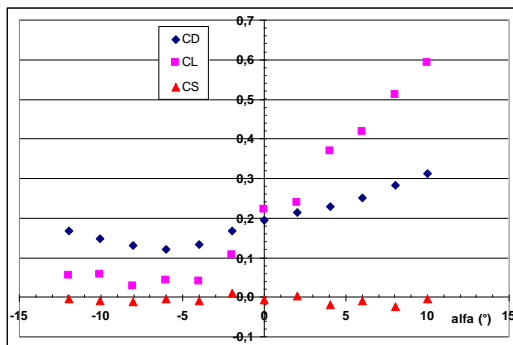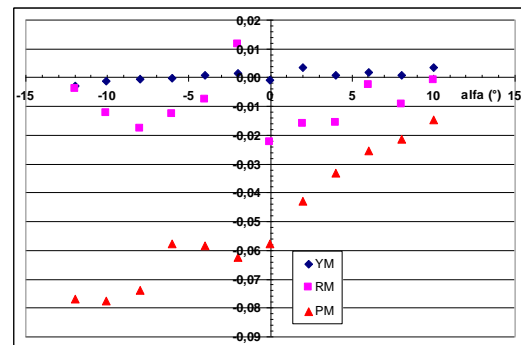
Fig. 9 Wind tunnel experimental setup

(a) Force coefficient, Re=6.8×10^5

(b) Moment coefficient, Re=6.8×10^5

(c) Force coefficient, Re=2.1×10^6

(d) Moment coefficient, Re=2.1×10^6

Fig. 10 Force and moment coefficients

Two Reynolds numbers were considered, namely Re=2.1×10^6 and Re=6.8×10^5. The angle of attach range was -12°≤α≤10°. The aerodynamic coefficients are presented without tare corrections while the blockage effect was taken into account. The tests were performed in a subsonic closed circuit wind tunnel with a circular test section having a diameter and a length equal to 3 m and 5 m, respectively. The diameter of the aircraft model is equal to 1 m (Fig. 9(a)). A sector of 30° was equipped by 120 static pressure taps distributed on the upper and lower surface along four radial directions equally spaced angularly by an angle of 10° (Fig. 9(b)). Some other taps were also added in intermediate points. The measurements of the pressure distributions around the complete
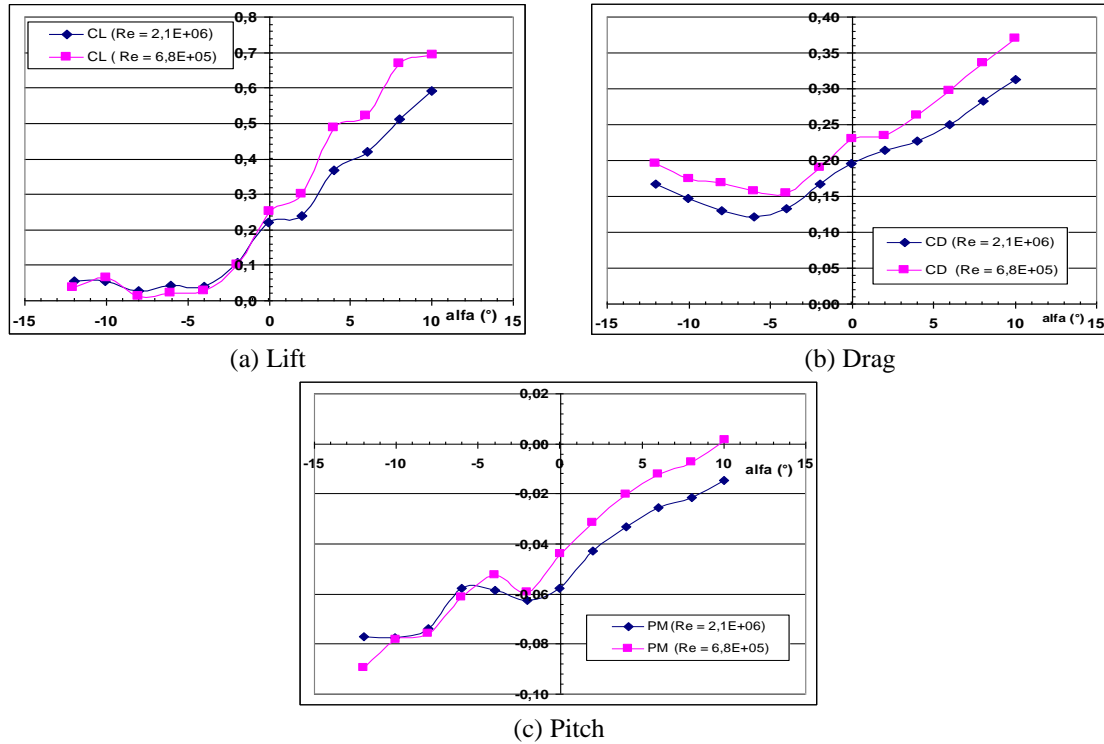
(a) Lift

(b) Drag

(c) Pitch

Fig. 11 Lift, drag and pitch curves

model were performed by the rotation of the model around its axis by steps of 30° each. A set of four Pitot tubes at the entry of the test section provided the measurement of the averaged dynamic pressure of the free stream. The plane view surface of the model was considered as the reference surface. The reference length is the diameter of the most external annuli. The moments measured are referred to the virtual center of the balance positioned nearly the top of the model support where its interface for the attachment of the model is present. This point is located approximately in correspondence of the center of the plane tangent to the lower part of the model where the support interface is attached to the model.

Forces and moments coefficients are shown in Fig. 10. For negative incidences, the lift coefficient is almost constant around 0.05 up to α=-4°. Then, the lift increases approximately linearly up to α=10°. The drag coefficient has a weak parabolic behavior for -12°≤α≤-2°. A nearly linear behavior was observed for 2°≤α≤10°, with a lower slope than the lift coefficient. Around the null incidence, the flow configuration can change significantly determining a complete different aerodynamic load redistribution around the body surface. It is likely that the flow interaction with the body changes considerably around zero incidences. Such change is due to the completely different geometry that characterizes the upper and lower parts of the aircraft. The drag coefficient is very high at negative incidences, around 0.18. For positive incidences, it increases up to 0.38. As expected due to the symmetrical shape of the body, the side force is absent for all the incidences. In the normal flight condition (i.e., negative incidences), the basic shape of the aircraft has very poor lifting characteristics and high drag. The pitching moment has a linear behavior with a switch at between -2°≤α≤-4°. The moment is always negative. A drastic change of the flow field

(a) α=0°, upper surface

(b) α=0°, lower surface

(c) α=-10°, upper surface

(d) α=-10°, lower surface
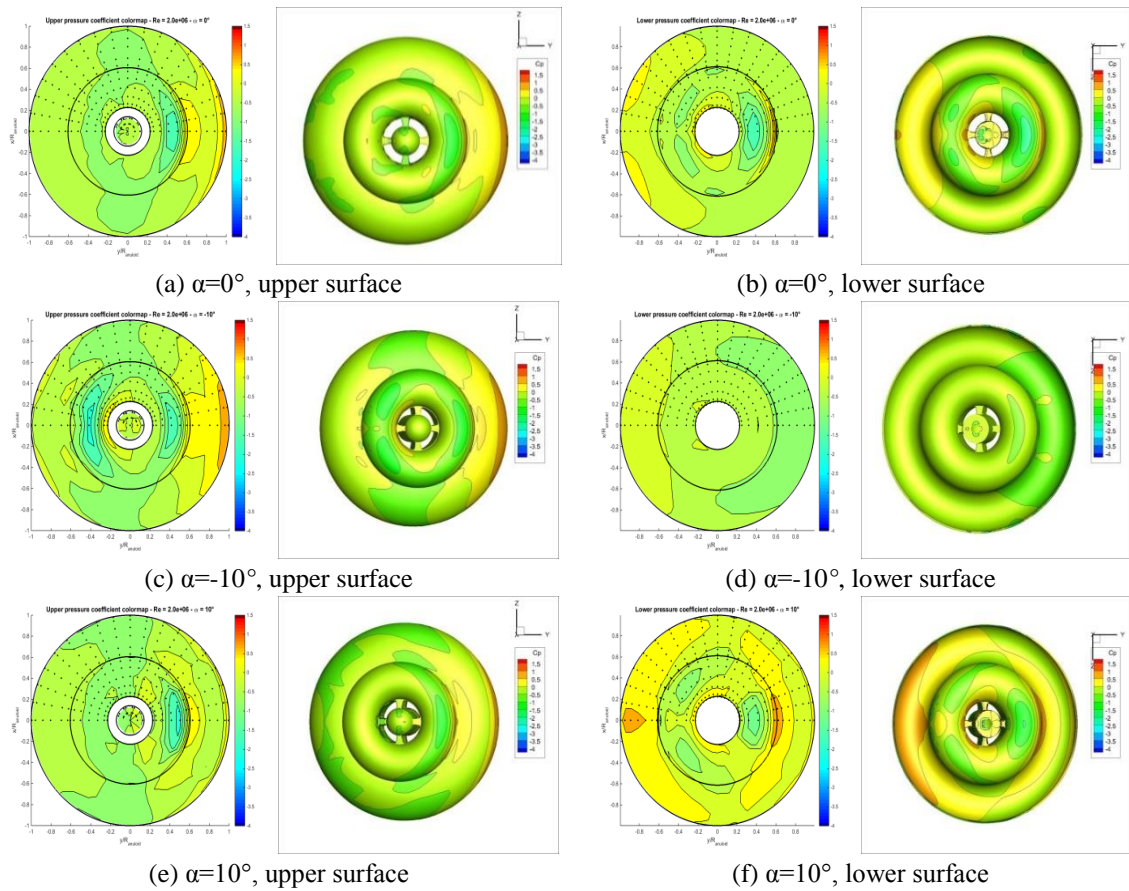
(e) α=10°, upper surface

(f) α=10°, lower surface

Fig. 12 Pressure distributions, wind tunnel (left) and CFD (right) results, Re=2.0×10^6

around the body could take place in the range of low incidences. This might explain the switching of the linear behavior. The yaw moment, as expected, is absent. While the rolling moment exhibits an oscillating behavior even though the values are low. For the higher Reynolds number, Re=2.1×10^6, the coefficients are similar to those of the lower Reynolds number. Lower drag is present. The behavior of the pitching moment for negative incidences is not linear as in the case of low Reynolds number with an oscillating behavior. For positive incidences, it remains linear and negative. An oscillating behavior in the whole range of incidences of the rolling moment is present, differently from the lower Reynolds number case. Such oscillations could be due to an asymmetric and not intrinsically stable 3D flow configuration that can take place around the model.

Fig. 11 shows the lift, drag and pitching moment curves. The lift curves for the negative range of incidence do not exhibit any sensitivity to the Reynolds number. A considerable Reynolds effects is instead present for the positive incidences. For the higher Reynolds number, the corresponding curve is characterized by lower lift. The drag curves behave similarly at the two Reynolds numbers. Moreover, at the higher Reynolds number, lower values of the drag are present for the whole range of incidence. The pitching curves behave as the lift curves. At negative incidence, there is no evidence of Reynolds effect, whereas it appears at positive incidences.
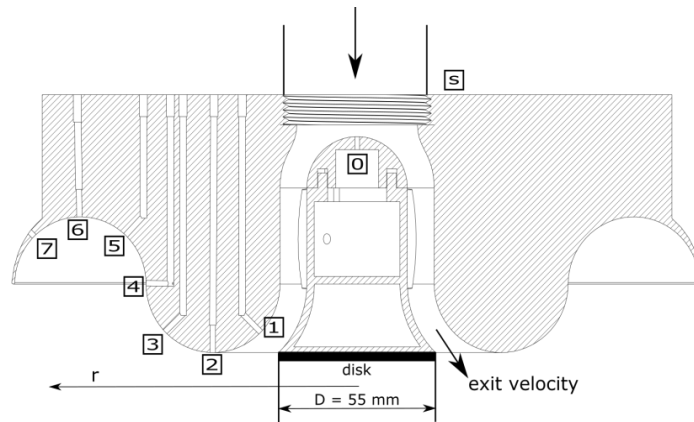
Fig. 13 Coanda effect analysis setup

4.2 Pressure distributions and CFD comparisons

The pressure distributions are presented as color maps of the pressure coefficient defined as

$$c_p = \frac{p - p_\infty}{1/2 \rho V_\infty^{\,2}} \tag{1}$$

The maps cover up to 210° pressure distributions around the model on both surfaces. The remaining parts are symmetrically duplicated. The following angles of attack were considered: $\alpha=0°$, $\alpha=-10°$ and $\alpha=10°$. The Reynolds number was set equal to 2.0×10^6. The CFD analysis considered the presence of the model support and the wind tunnel wall.

Fig. 12 shows the results for both body surfaces. Wind tunnel (left) and CFD (right) pressure distributions are shown. A good match was found. Furthermore, highly three-dimensional features of the flow field for all the incidences were found. Constant pressure regions are present, and this suggests the existence of large regions of separated flow. Also, such a flow behaviour is present inside the curved cavity of the lower fore body part. These pressure distributions could be also associated with the presence of a vortical structure positioned inside the rounded cavity. For $\alpha=-10°$, the lower part has almost completely separated flows. A region of high pressure is present for positive incidences on the bump of the lower surface. On the upper surface, for all the incidences the pressure maps appear almost similar to each other. In particular, high pressure takes place in front of the body in the stagnation region and a low-pressure region ($c_p\approx-2$) is located in front of the upper bump. A region of largely separated flow is present from the fore part of the fan inlet and develops in the rear part. It covers an azimuthal sector $\theta=\pm45°$ with respect to the symmetry plane starting from the aft part. This separated flow region is also unsteady and characterize almost all the tested incidences.

4.3 Analysis of the Coanda effect

A simplified, reduced scale (1:22) model of the aircraft was considered to characterize the Coanda effect on the lower surface. The characterization of the Coanda effect is necessary to evaluate the possibility of maneuvering the aircraft using the movable curved surfaces positioned
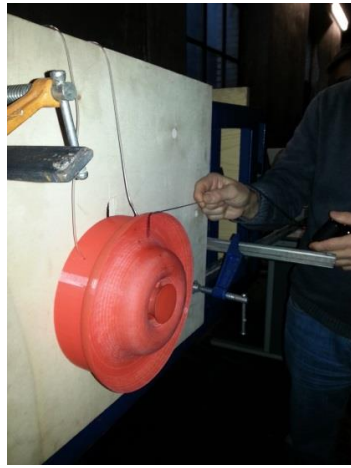
(a) Original geometry   (b) Modified geometry

Fig. 14 Coanda effect experimental setup

(a) *D*=52 mm   (b) *D*=62 mm

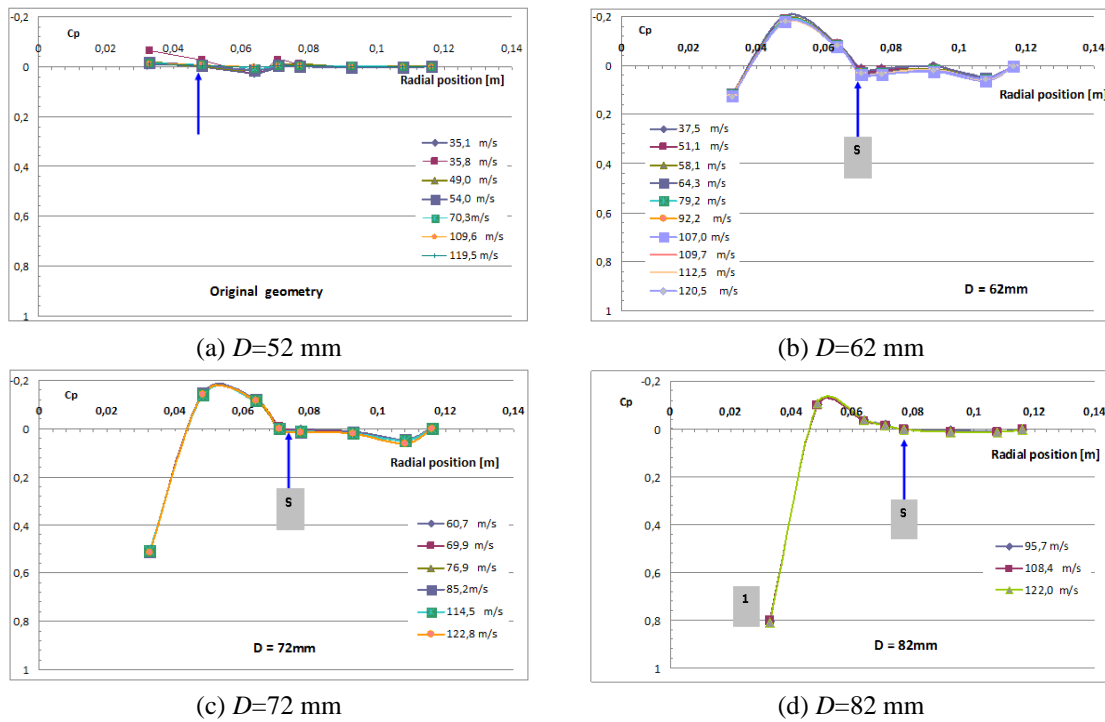(c) *D*=72 mm   (d) *D*=82 mm

Fig. 15 Pressure distributions along the lower surface of the aircraft, the blue arrow indicates the flow separation point

at the annular exit of the duct fan. The maneuverability of the aircraft is based on the change of the load distributions on the lower curved surface. Such change is generated by the asymmetric flow behavior supposed to be introduced by the curved movable surfaces that would allow the flow to remain always attached to the lower curved surface characterized by a change of the curvature. In

(a) *D*=52 mm

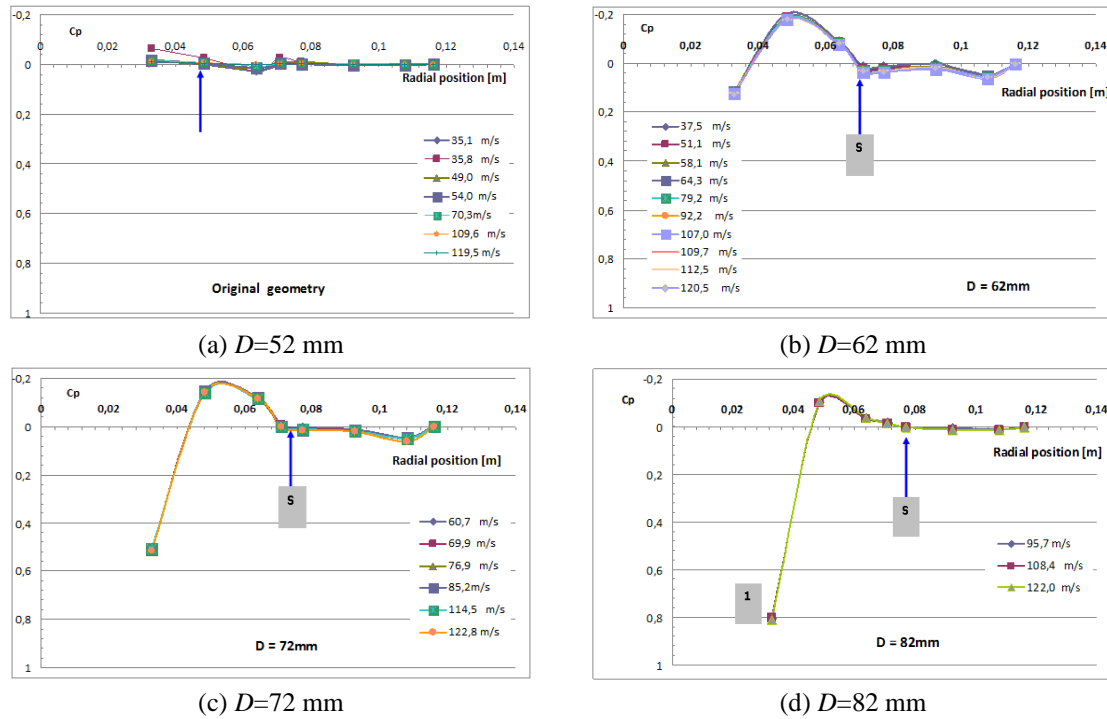(b) *D*=62 mm

(c) *D*=72 mm

(d) *D*=82 mm

Fig. 15 Pressure distributions along the lower surface of the aircraft, the blue arrow indicates the flow separation point
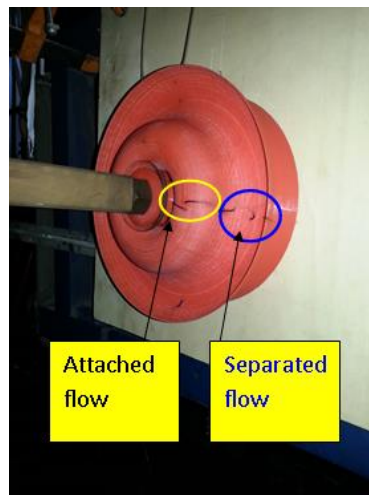

Fig. 16 Tuft flow visualization for the modified base, *D*=62 mm

Fig. 13, the drawing of the cross section of the model with the pressure taps is shown. The lower part of the model matches the scaled geometry of the aircraft. On the other hand, the upper part is flat. The upper side was, in fact, used to fasten the model to a large flat plate, see Fig. 14(a). A jet of compressed air was injected from the top inlet part of the model using a metallic tube connected
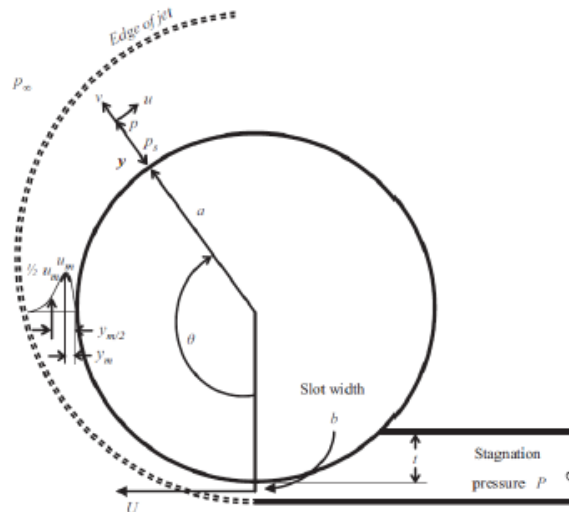
Fig. 17 Coanda effect around a cylinder (Newman 1961)

through a thread with the model inlet. The cross flow was not considered. The mass flow rate was varied through a regulation valve. Two pressure taps were also mounted for the measurements of the jet velocity. The first one was located on the top of the engine hub curved in correspondence of the stagnation point. The second one was positioned on the inlet tube wall as a static pressure tap. A multi-manometer with very long flues was used for the measurements of the pressure distributions. Various mass flow rates were considered allowing inlet velocities ranging from around 35 m/s up to 100 m/s. Some modifications of the exit geometries were also tested to evaluate the effects of different cross sections exit on the pressure distributions, see Fig. 14(b). Various disks having different diameters were mounted on the base of the original configuration, namely D=52 mm, D=62 mm, D=72 mm, and D=82 mm. In particular, the smallest diameter represents the original geometry. Various positions of the disks with respect to the axis of the central body were tested to simulate some orientations of the exit curved movable surfaces.

The Coanda effect is driven by the balance between the centrifugal force and radial pressure force around the curved surface. According to this balance, the flow is attached where the local pressure, p_s, is lower than the ambient pressure where the jet is injected. In this experiment, this pressure is equal to the ambient pressure acting on the exit flow. Where the values of the two pressures are equal, the flow separation takes place. Such criterion assumed to identify the separation in the present investigation. According to the definition of the pressure coefficient, the flow separation is located where the pressure coefficient is equal to zero.

Pressure distributions for different exit velocities and diameters are shown in Fig. 15, whereas flow visualizations are given in Fig. 16. The pressure corresponding to the tip rounded surface (radial position=0.12 m) was imposed equal to the ambient pressure. The original configuration has almost constant values of pressure along the curved surface. Such a distribution is typical of separated flows. In other words, the flow is separated from the second pressure tap, corresponding to a value of the angle $\theta \approx 50°$, up to the end of the lower surface. The origin of the angle θ is at the exit section of the annular gap.

It can be stated that the absence of attached flow on the lower surface excludes the presence of the Coanda effect on that surface. As observed from the previous pressure distributions presented
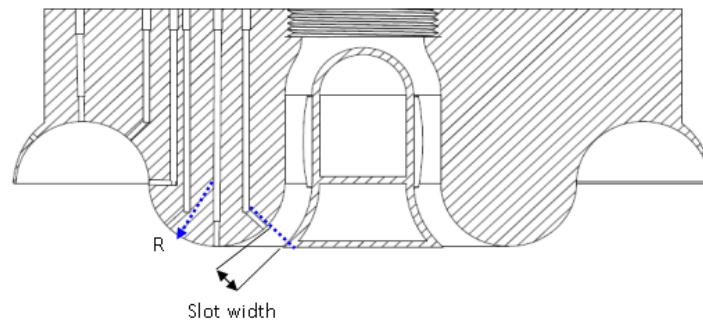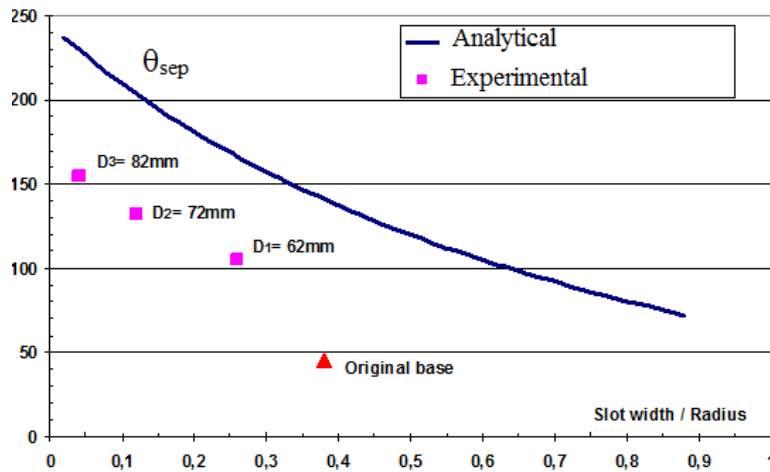
Fig. 18 Evaluation of the separation angle

Fig. 19 Estimation of the flow separation and comparison with an analytical (Newman 1961)

before the flow behavior is greatly influenced by the base exit geometry and also by the shape of the curved lower surface. An increase of the base diameter leads to a reduction of the exit section. A blockage effect takes place inside the curved duct and produces higher pressures for the most internal measurement point (tap n.1). The value of the velocity exit was kept nearly constant by increasing the upstream pressure through the regulation valve. Moreover, the presence of the disk modifies the flow direction at the exit. In fact, larger base diameters enable the "curved Coanda surface" at the exit. The flow attaches quickly to the rounded surface remaining attached up to some local critical flow conditions that take place. It can be stated that the most critical point around the lower surface is where the shape changes its curvature. In fact, more often than not, the flow remains attached up to the inflectional point, at least for the test conditions considered.

A study focused on the Coanda effect was proposed by Newman (1961). A simple model was considered with a turbulent jet from a slot and evolving around a 2D cylinder, see Fig. 17.

The model describes the separation angle, θ, as a function of the ratio between the slot width (b) and the cylinder radius (a),

$$\vartheta_{sep} = 245 - 391 \frac{b/a}{1 + 9/8 * b/a} \tag{2}$$

Table 2 Effect of the disk shifting on θ_{sep}, *D*=72 mm

Shifting	θ_{sep}	*b*	*b/a*
-	139.7	3	0.133
d_s = 3 mm			
dx	119.4	3.2	0.142
sx	139.9	3.2	0.142
up	138.3	2	0.089
down	78.73	4.5	0.2
down + dx	124.9	4.8	0.213
up + dx	136.4	2.2	0.098
down + sx	119.4	3.2	0.142
up + sx	139.9	3.2	0.142
d_s=6 mm			
dx	135.6	3.5	0.156
sx	135.6	3.5	0.156
up	131.7	0.8	0.0356
down	129.6	6.5	0.289
down + dx	157.4	6.8	0.302
up + dx	132.9	1	0.044
down + sx	159.0	6.8	0.302
up + sx	122.9	1	0.044

Table 3 Effect of the disk shifting on θ_{sep}, *D*=62 mm

Shifting	θ_{sep}	b	b/a
-	127.6	6.2	0.276
d_s=3 mm			
dx	127.5	6.5	0.289
sx	127.5	6.5	0.289
up	143.7	4	0.178
down	85.93	8	0.356
down + dx	159.5	8.5	0.378
up + dx	138.4	4.5	0.2
d_s=6 mm			
dx	149.9	6	0.267
sx	152.9	6	0.267
up	142.9	2.5	0.111
up + dx	141.8	3	0.133
up + sx	143.8	3	0.133

An estimation of the slot width "*b*" for the various geometric configurations tested was evaluated. The angle θ_{sep} was evaluated from the pressure distributions according to the assumed
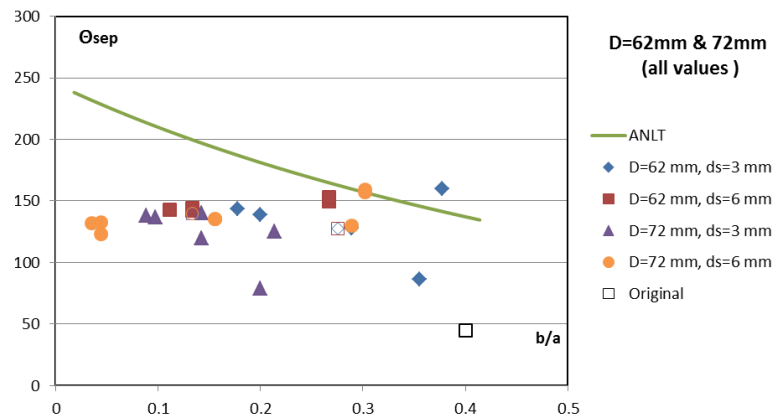
Fig. 20 Effect of the asymmetric disk shifting on the separation angle

criteria. The origin of the angle is the exit section. In Fig. 18, the indicated slot width evaluation is shown. As can be observed in Fig. 19, the separation angles of the modified base geometry follow the same trend of the separation angle of the cylinder. The lower values of the separation angle in the case of the Anuloid model are essentially due to the different geometry between the two cases. Moreover, as the ratio width slot/radius decreases (i.e., D increases), the angle of separation increases.

The effects of the movable surfaces were modeled by shifting the disk along the two orthogonal directions. One movement in the direction of the pressure taps (referred to as up and down movements) and the other one in the direction perpendicularly (referred to as left and right movements). It has to be remarked that the pressure distributions were evaluated only at locations of the taps present on the model. The complete investigation should have had pressure taps all around the lower surface. As a consequence, the flow separation angle evaluated in this investigation is always referred to the plane of measurement. Only two disks were considered, (D=62 mm and D=72 mm). Two shifts were considered, d_s=±3 mm and d_s=±6 mm. The effect is shown in Tables 2 and 3 and Fig. 20. The disk shift influences the pressure distributions according to the amount of the displacement and the direction of the shifting. In particular, some shifting considerably change the angle of separation (up and down movements) while the others (left and right movements) do not modify the flow separation angle significantly as expected. The base shifting greatly influences the whole flow field introducing very complex three-dimensional features.

It can be concluded that the Coanda effect has been obtained in this simple experiment. As the CFD results also evidenced, this new concept of maneuverability could be therefore exploited on a real aircraft configuration.

5. Conclusions

This paper has presented the main outcomes that stemmed from the aerodynamic analysis of an innovative disk-shaped VTOL aircraft, the Anuloid. This aircraft is conceived for emergency operations and civil transportation in urban areas. The Anuloid should lower noise pollution (due to the ducted engine) and have wider operational scenarios than existing VTOL.

The aircraft is based on the following main characteristics: The lift for take-off and cruise is provided by a fan that is powered by a turboshaft; the anti-torque is provided by a system of fixed and swiveling radial vanes by controlling the swirl of the flow that outgoes from the engine fan; the flight control is obtained by means of the radial vanes and the individually swiveled circumferential vanes.

The results presented in this paper deal with the CFD analyses of the horizontal and vertical flight, and the wind tunnel testing. The aim of these investigations was the investigation of the main physical capabilities of the aircraft to highlight the critical points to be further investigated in the next phases of the design.

The main results are the following:

• The Coanda effect is continuously present at the lower surface of the Anuloid during the steady vertical, and horizontal flight and the horizontal acceleration for the both examined angles of attack as well. Although the Coanda effect does not provide significant lift, its presence is fundamental to the control of the aircraft.

• For negative incidences, the model develops very low lift and very high drag.

• The behavior of some aerodynamic coefficients, namely the lift, drag and rolling moment, change their trend around $\alpha=0°$ drastically. This suggests that a great variation of the flow topology around the body and especially on the lower side can take place.

• The pressure maps highlights very complex 3D flow developing around the model.

Some guidelines and recommendations can be drawn for the future developments of this aircraft. The main aerodynamic Anuloid potential issue, indicated by the CFD analysis, seems to be very high drag, but the magnitude of this drag must be validated in future in wind tunnel with a model with fully functioning rotor and with functioning wall jet (Coanda effect). To support efficiently the Coanda effect on the lower annular cavity some active flow control techniques can be taken into consideration. For example, the suction or the presence of synthetic jets appropriately positioned and oriented can maintain the flow attached along all the curved surface.

Acknowledgments

References

Angle, G., O'Hara, B., Huebsch, W., Smith, J., Joslin, R.D. and Jones, G.S. (2006), "Experimental and computational investigation into the use of the Coanda effect on the bell A821201 airfoil", *Progr. Astronaut. Aeronaut.*: *Appl. Circul. Contr. Technol.*, **214**, 277-292.

Barlow, C., Lewis, D., Prios, S.D., Odedra, S., Erbil. M.A., Karamanoglou, M. and Collis, R. (2009), "Investigating the use of Coanda effect to create novel unmanned aerial vehicles", *Proceedings of the International Conference on Manufacturing and Engineering Systems*.

Crivoi, O., Doroftei, I. and Adascalitei, F. (2013), "A survey of unmanned aerial vehicles based on Coanda effect", *Tehnom. J.*, **20**, 338-344.

Fite, E.B. (2013), "Ducted and unducted fans in airbreathing engines", *Encyclop. Aerosp. Eng.*, 1-14.

Lindenbaum, B. and Blake, W. "The VZ-9 'Avrocar'", www.robertcmason.com/textdocs/avro-car-VZ9.pdf.

Newman, B.G. (1961), *The Deflection of Plane Jets by Adjacent Boundaries-Coanda Effect, Boundary*

Layer and Flow Control, Pergamon Press, Oxford, 232-264.

Petrolo, M., Carrera, E., D'Ottavio, M., De Visser, C., Patek, Z. and Janda, Z. (2014), "On the development of the anuloid, a disk-shaped VTOL aircraft for urban areas", *Adv. Aircraft Spacecraft Sci.*, **1**(3), 353-378.

Petrolo, M., Carrera, E., De Visser, C., D'Ottavio, M. and Polit, O. (2017), "Further results on the development of a novel VTOL aircraft, the Anuloid. Part II: Flight mechanics", *Adv. Aircraft Spacecraft Sci.*, **4**(4), 421-436.

EC